INFLUENCE OF SECONDARY AIR ON THE FLOW FIELD OF NGZF CLASSIFIER

Ziwei Zhao, Chenxi Hui, Jiaxiang Peng, Ying Fang*

College of Materials Science and Engineering, Nanjing Tech University, Nanjing, 211816, China

** E-mail: powderfang@163.com or powder8817@njtech.edu.cn*

Abstract: Aiming at the problems of uneven material dispersion of traditional air classifier, NGZF classifier with downward air inlet fabric method is designed. In order to investigate the classification law of the classifier and the effect of secondary air on the flow field of the classifier, this paper utilizes ANSYS-Fluent19.2 software to simulate the internal flow field and conducts material experiments using the response surface method. The simulation results demonstrate that with the rise of the secondary air volume, the overall flow field distribution tends to be appropriate, and the washing flow field created by the secondary air does not interfere with the primary flow field. However, when the secondary air is too big, it will generate turbulence in the axial velocity in the guide cone zone. The discrete phase model (DPM) indicated that the secondary air would re-screen the misclassified fine particles. Response surface experiments with calcined petroleum coke showed that by setting the cut particle size at 50 μm and maximizing the classification accuracy, the ideal operating parameters were a rotor speed of 1037.4 rpm, a primary air volume of 429.6 $m^3 \cdot h^{-1}$, and a secondary air volume of 50.2 $m^3 \cdot h^{-1}$. This work not only provides a novel approach for the design and development of airflow classifiers but also gives theoretical direction for their implementation in industrial production.

Keywords: Air classifier, CFD, Secondary air, Performance optimization, Response surface methodology

1. INTRODUCTION

With the fast growth of powder technology, the powder is extensively employed in the chemical industry, medicine, metallurgy, national defense, and other industries because of its distinctive features. Powder classification is the process of classifying powder particles into two or more components, which is a crucial process link in many industrial processes. Industrial powder classification may be separated into dry classification and wet classification.[1, 2] The NGZF classifier is one form of dry classification equipment, and its construction is given in Fig. 1.

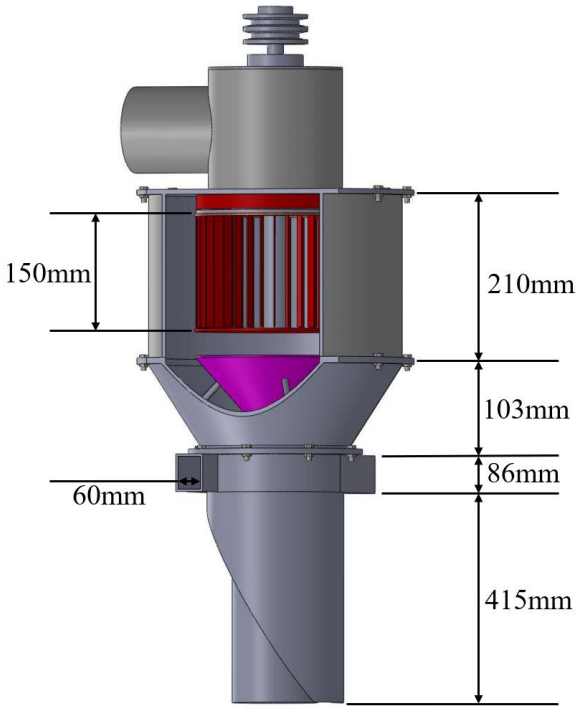

Fig. 1 Three-dimensional structure of NGZF air flow classifier.

With the fast growth of Computational Fluid Dynamics (CFD), the modeling of vortex classifiers has garnered extensive interest. Some academics have explored the matching of operational parameters to enhance classification performance by applying simulation and modeling approaches.[3-6] In addition, some researchers have also investigated the structure of the rotor cage, worm shell, and air inlet, and the reasonable construction increases the stability of the flow field, which improves the classification efficiency and classification accuracy of the classifier.[7-15] Yu et al. [16] for the acquire a well-distributed and uniform flow field of the turbo air classifier, a guide vane design approach is presented based on the airflow trajectory in the worm shell, and a new guide vane with a 10-degree setting angle at 12-1200 operating circumstances is created. The numerical simulation results reveal that the standard deviation of circumferential radial and tangential velocities is minimized. In addition, the trajectories of particles of the same size at different circumferential points demonstrate that their classification findings are consistent. Yu et al.[17] simulated the effect of the inlet layout of a vertical turbine air classifier on the distribution of the flow field and the trajectory of the particles, and found that the adjustment of the air inlet can increase the axial velocity and turbulence dissipation rate at the inlet, improve the material conveying and dispersing ability, and effectively eliminate the vortex in the channel of the rotor cage. Yu et al.[18] suggested enhancing the guide vane of a turbo air classifier by suggesting that the cylindrical tail of the guide vane accelerates the dispersion and improves the powder dispersion. However, with the rising need for capacity as well as the requirement for refinement, various challenges have developed in the industrial manufacture of turbo air classifiers.[19-21] Due to the asymmetry of the classifier structure and airflow supply, the gas velocity at the inlet and the worm shell is too large, resulting in an unstable flow field of the classifier, localized accumulation of ash, and greater wear on the guide vanes.[13, 22] Xu et al.[23] upgraded the air inlet duct and advocated that the use of clean air access for classifier air will avoid the problem of dust collection in the air duct. However, because of the structural limits of the classifier itself, it did not substantially fix these difficulties. To fundamentally overcome the difficulties, Mou et al.[24-26] constructed a new type of high-efficiency rotor classifier and optimized its structure using CFD, although this classifier

did not feature a secondary air inlet. In the real classification, there is often a circumstance in which coarse powder contains fine powder.

Most of the fine powder included in the coarse powder is created by the agglomeration of particles, tiny particles linked to big particles, and small particles entrapped in the process of descending large particles. The secondary air can substantially help this issue. At present, most of the classifiers are used in the "primary flow field + washing flow field" mode, the secondary air can not only improve the dispersion of particles but also can be misclassified particles for the second separation, to improve the classification accuracy of the classifier plays an important role. In addition, adjusting the secondary air volume can also change the cut size, which enriches the adjustment means of cut size. Some researchers have experimentally researched the ratio of secondary air volume and primary air volume of the classifier, and some researchers have experimentally studied the ideal operating parameters of the classifier. Sun et al.[5] researched the matching of rotor speed, primary air volume, and secondary air volume, and determined that the particle cut size (d_{50}) is more sensitive to rotor speed and primary air volume than secondary air volume, and there is a weak interaction between them. The classification accuracy *K* is substantially impacted by each operational parameter, and the ideal operating parameters are established. Braun et al.[27] observed that a sufficient ratio of secondary air and primary air helps to minimize the fishhook effect. Zeng et al.[28] experimentally determined that the classification accuracy of the classifier was greatest when the ratio of secondary air volume to primary air volume was 0.168. However, the internal flow field and particle motion of the classifier have not been extensively examined, and the action mechanism of the washing flow field has not been systematically elucidated.

Therefore, in this research, the CFD simulation approach was employed to model the airflow in the NGZF classifier using ANSYS-Fluent 19.2 software. The influence of secondary air on the flow field of the rotor classifier is researched, and material tests are undertaken to improve the operating parameters of the classifier using the response surface approach. This work not only presents a novel NGZF classifier but also gives theoretical direction for the design and optimization of vertical rotor air classifiers.

2. CALCULATION METHODOLOGY

2.1 Description of the equipment

The three-dimensional construction of the combined airflow classifier is presented in Fig. 2. It comprises a V-type classifier and an NGZF classifier. The major role of a V-type classifier is to reclassify and distribute the materials. The NGZF classifier is the primary site of material classification. The feeding mode of the NGZF classifier is downward feeding, adopting airflow conveying, and the bottom-feeding pipe has a suitable cross with the coarse powder recovery region, to increase the space utilization rate. The secondary air inlet is introduced in the coarse powder recovery region to generate the washing flow field, which can classify the falling coarse powder again and guarantee that the classifier has high classification accuracy. Compared with the typical turbine air classifier, the NGZF air classifier just needs to cause the rotor cage to rotate, which effectively minimizes the energy consumption of the classifier.

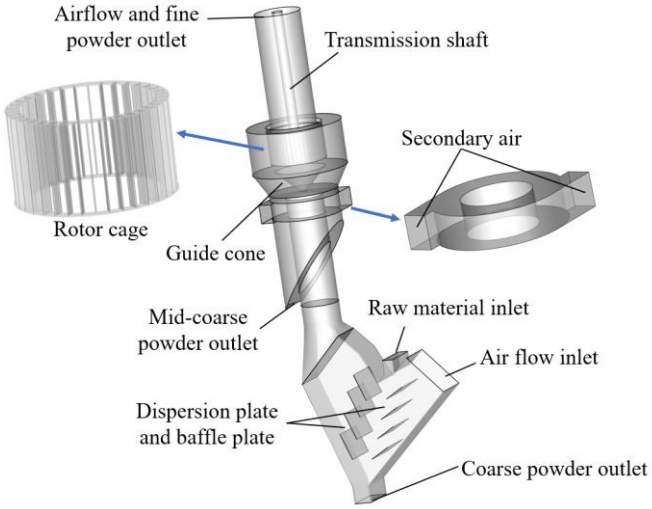

Fig. 2 Combined Airflow Classifier.

The secondary air present in the NGZF classifier does not impact the flow field of the static classifier. Therefore, in the following study, the simulation analysis is largely carried out on the NGZF air classifier. The operating concept of the NGZF air classifier is as follows: following the pre-dispersion and pre-separation of the V-type classifier, the material enters into the NGZF classifier with the airflow, and then it arrives at the guide cone region to strike the guide cone for dispersion. Due to the large mass of the coarse particles, some of the coarse particles decrease in velocity under the influence of inertia and collision, move toward the cylinder wall, and subsequently settle along the outer wall of the cylinder. The remaining particles continue to climb to the classification chamber, The rotor rotates at high speed to drive the particles and classify them. At this time the particles are subject to air resistance, centrifugal force, and gravity. Coarse particles with significant masses are separated from the airflow and strike the wall of the classifying chamber, losing velocity and downward. Fine particles with tiny masses will enter the rotor cage and be ejected through the fine powder exit. However, the downward particles are re-graded in the coarse powder recovery area, where the fines rise to the classification chamber. Eventually, they are collected as coarse and fine powder respectively.

2.2 Model establishment and mesh generation

The classifier was designed and meshed using SolidWorks and ICEM, respectively. To assist the computation, the construction of the NGZF classifier is fairly simplified, as illustrated in Fig. 3a. It is split into seven sections, from top to bottom, which are fine powder outlet, rotor cage, classifying chamber, guide cone, secondary air inlet, coarse powder outlet, and air inlet. Among them, the diameter of the fine powder outlet is 190mm; the height of the rotor cage is 150mm, the diameter is 260mm, there are 36 blades evenly distributed on the rotor cage, each blade is 2mm thick and 20mm wide; the height of classification chamber is 210mm, the diameter is 440mm; the height of guide cone is 103mm, the diameter is 234mm; the height of secondary air inlet is 86mm, the width is 60mm; the diameter of air inlet is 175mm. Due to the heterogeneous structure of the coarse powder outlet, a tetrahedral unstructured mesh was used, while a hexahedral structured mesh was used for the rest of the section. The mesh quality of the coarse powder outlet is 0.4 or more and the mesh quality of the remaining parts are 0.7 or more. To ensure the correctness of the computation results, it is required to independently verify the number of split meshes. Four distinct mesh quantities, 1084932, 1570063, 2072752, and 2501904, were examined. Under these four grid numbers, points are obtained on the outside surface of the rotor cage to determine its radial velocity distribution as illustrated in Fig. 3b. It can be observed in the image that when the number of meshes reaches 2072752, the

radial velocity distribution no longer varies, showing that this number of meshes meets the mesh-independence criteria.[3] Therefore, 2072752 meshes are employed for simulation in this work.

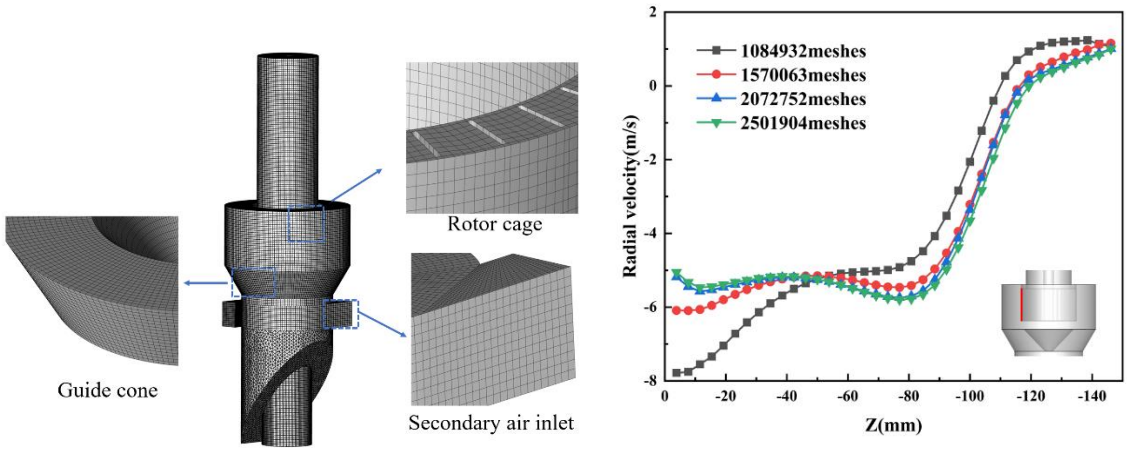

(a) **(b)**

Fig. 3 Meshes of the NGZF classifier (a) and radial velocity distribution for different mesh numbers (b).

2.3 Turbulence model and simulation conditions

In this paper, ANSYS Fluent 19.2 is utilized for 3D steady-state simulations. For incompressible gas flow, the mass and momentum equations are as follows[29]:

$$\frac{\partial u_i}{\partial x_i} = 0 \tag{1}$$

$$\rho u_j \frac{\partial u_i}{\partial x_j} = -\frac{\partial p}{\partial x_i} + \frac{\partial}{\partial x_j}\left[u\left(\frac{\partial u_i}{\partial x_j} - \frac{\partial u_j}{\partial x_i}\right)\right] - \rho\frac{\overline{\partial u_i' u_j'}}{\partial x_j} \tag{2}$$

Where ρ is the airflow density; u_i is the gas velocity; x_i is the position; μ is the airflow viscosity; p is the static pressure; $-\rho\frac{\overline{\partial u_i' u_j'}}{\partial x_j}$ is the Reynolds stress term.

The Reynolds Stress Model (RSM) has been shown to be a suitable model for describing anisotropic flow in air classifiers. It allows for a more accurate prediction of the turbulent flow structure and pressure drop inside an air classifier.[3, 30] The transport equation for Reynolds stress can be written as[31]:

$$\frac{\partial}{\partial t}\left(\rho\overline{u_i u_j}\right) + \frac{\partial}{\partial x_k}\left(\rho U_k \overline{u_i u_j}\right) = D_{ij} + \varphi_{ij} + G_{ij} + \varepsilon_{ij} \tag{3}$$

$$D_{ij} = -\frac{\partial}{\partial x_k}\left(\rho\overline{u_k u_i u_j} + \overline{pu_j}\delta_{ik} + \overline{pu_i}\delta_{jk} - \mu\frac{\partial}{\partial x_k}\overline{u_i u_j}\right) \tag{4}$$

$$\varphi_{ij} = \overline{p\left(\frac{\partial u_i}{\partial x_j} + \frac{\partial u_j}{\partial x_i}\right)} \tag{5}$$

$$G_{ij} = \rho\left(\overline{u_i u_k}\frac{\partial U_j}{\partial x_k} + \overline{u_j u_k}\frac{\partial U_i}{\partial x_k}\right) \tag{6}$$

$$\varepsilon_{ij} = 2\mu\frac{\partial u_i}{\partial x_k}\frac{\partial u_j}{\partial x_k} \tag{7}$$

The two terms on the left side of equation (3) are the time rate of change of the Reynolds stress and the convection term, respectively. The four terms on the right-hand side are the diffusion term D_{ij}, the pressure-strain term φ_{ij}, the stress-generation term G_{ij}, and the turbulent dissipation term ε_{ij}. D_{ij} occurs as a dispersion and is conservative. It consists of three parts: the turbulent diffusion term, the pressure diffusion term, and the viscous diffusion term. φ_{ij} consists of the turbulent pressure and the turbulent strain, and is also known as the Reynolds stress redistribution term. G_{ij} denotes the interaction between the

Reynolds stress and the mean flow gradient, which enhances the source of the Reynolds stress.ε_{ij} consists of the fluid viscosity coefficient and the turbulent velocity gradient, and its primary function is to dissipate the turbulent energy.

The wall borders are treated with no-slip boundary conditions while the near-wall surfaces are treated with normal wall functions. The rotor cage is simulated using a multi-reference system model. The rotor cage rotation direction is set to clockwise and the rotational speed is 800 rpm. The pressure-velocity coupling is accomplished using the SIMPLEC method and the convection and diffusion are performed using the QUICK difference scheme. There are three inlets and two outlets in the classifier, the boundary conditions of the primary air inlet and secondary air inlet are set as "velocity-inlet", the boundary conditions of the fine powder outlet are set as "outflow", and the outlet of the coarse powder in the industrial application is usually closed, so its boundary conditions are set as "wall". The fine powder outlet discrete boundary condition is set as "escape", the coarse powder outlet discrete boundary condition is set as "trap", and the remainder of the wall discrete boundary conditions are set as "reflect".

2.4 Discrete Phase Model

The discrete phase model is used on the assumption that the volume of particles in the classification is within 10% of the entire fluid domain.[15, 32] In the discrete phase model, steady state tracking of the discrete phase model is performed to predict the trajectory of the particles. When the flow field reaches a steady state, the particles are integrated when the continuous phase iterations reach convergence. A series of particle states with integration time steps can be obtained under continuous flow field conditions. A series of particle positions can be connected to a motion trajectory. The steady-state tracking method is suitable for single-phase coupling calculations, and after obtaining a stable flow field, a discrete phase model is added to calculate the trajectory. The particle motion equations are as follows:

$$\frac{d\vec{u}_P}{dt} = F_D(\vec{u} - \vec{u}_P) + \vec{g}\frac{(\rho_P - \rho)}{\rho_P} \tag{8}$$

Where $\vec{u}_P$ is the particle velocity, t is the time, $\vec{u}$ is the the gas velocity, $\vec{g}$ is the gravitational acceleration, ρ_P is the particle density, ρ is the fluid density. F_D is the drag force, is given by

$$F_D = \frac{18\mu}{\rho_P {D^2}_P}\frac{C_D Re_P}{24} \tag{9}$$

$$Re_P = \frac{\rho D_P |\vec{u}_P - \vec{u}|}{\mu} \tag{10}$$

Where μ is the molecular viscosity of the gas, D_P is the particle diameter, C_D is the drag coefficient. Re_P is the relative Reynold number.

3. SIMULATION RESULTS AND ANALYSIS

3.1 Overall flow field distribution

The airflow movement route in the NGZF classifier is depicted in Fig. 4. Fig. 4a depicts the airflow route formed by the joint action of the primary air and the secondary air, and their respective pathways are depicted in Fig. 4b and Fig. 4c. The primary air enters from the primary air inlet, deflects into the rotating cage through the guide cone, and flows out from the fine powder outlet. The secondary air arrives from the secondary air inlet, which can wash the particles again and decrease particle entrapment. The two merges at the guide cone area. It can be seen that the primary air and secondary air into the classifier after the emergence of the obvious phenomenon of close partition control, that is, the primary air occupies the center area, the secondary air occupies the peripheral area, the overall distribution of the flow field is very regular. In addition, this flow field distribution structure maximally avoids the mutual interference of the primary

flow field and the washing flow field. By controlling the gas speed or air volume of the primary air and the secondary air separately, the adjustment of the strength of the respective flow field can be realized.

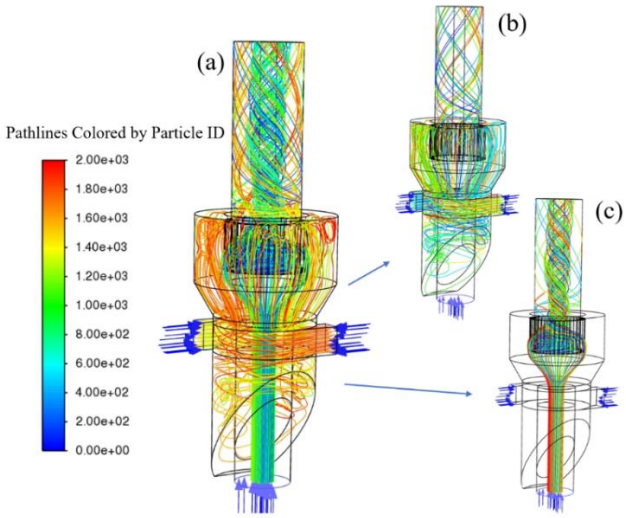

Fig. 4 NGZF classifier flow field.

As illustrated in Fig. 5, a low-speed vortex is produced at the top of the classification chamber to wash the descending coarse powder. Swirls are also created near the bottom of the rotor cage, due to a structural dead zone that cannot be avoided but can be reduced by structural changes. In the coarse powder recovery region, an outer downward and inner upward airflow is created. The guide cone below the rotor cage has two tasks, one is to divert the airflow into the classification chamber and to avoid direct impact of the airflow on the bottom of the rotor cage. Secondly, the material will touch the guide cone when carried by the airflow, which allows the material to be dispersed.

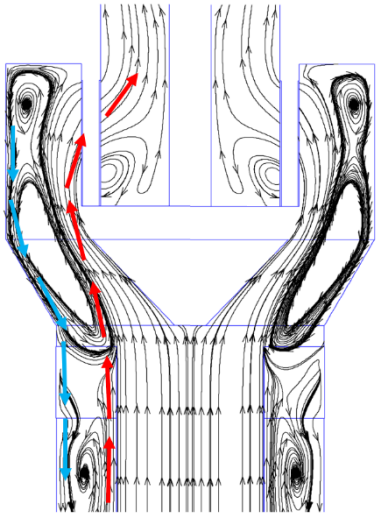

Fig. 5 Airflow movement in the NGZF classifier.

3.2 Velocity distribution in the NGZF classifier

3.2.1 Tangential velocity distribution

The rotor cage region is the major zone for powder classification, hence it is vital to study its velocity field. The tangential gas velocity is responsible for the cyclonic flow and centrifugal force of the particles, which is principally brought about by the high-speed spinning of the rotor cage.[33] Fig. 6(a) illustrates the tangential gas velocity distribution in the top half of the classification chamber and rotor cage. The tangential gas velocity in the classification chamber is 0 m/s when the secondary gas velocity is 0-6 m/s, whereas the classification chamber produces a tangential gas velocity of roughly 1 m/s when the secondary gas velocity

is 8 m/s. The stability of the tangential gas in the classification chamber is highly critical for the classification process, and the addition of the secondary air did not alter the stability of the airflow in the classification chamber. The tangential gas velocity steadily rose after entering the rotor cage, but the volume of the secondary air did not alter the tangential gas velocity in the rotor cage. Fig. 6(b) illustrates the tangential gas velocity distribution near the edge of the rotor cage. The tangential gas velocity changes substantially in the bottom portion of the rotor cage and is practically constant in the middle and higher regions, but when the secondary air is too big, the tangential velocity swings in a limited range, which has an undesirable influence on the classification. From the middle and lower section of the rotor cage, the tangential gas velocity steadily increases, which is created by the vortex of the high-speed rotation of the classification chamber. As illustrated in Fig. 6(c), the tangential gas velocity in the secondary air region rises with the secondary air, and the velocity increases the closer it is to the outer wall surface. The tangential gas velocity here can carry out a second classification of particles and increase the classification accuracy.

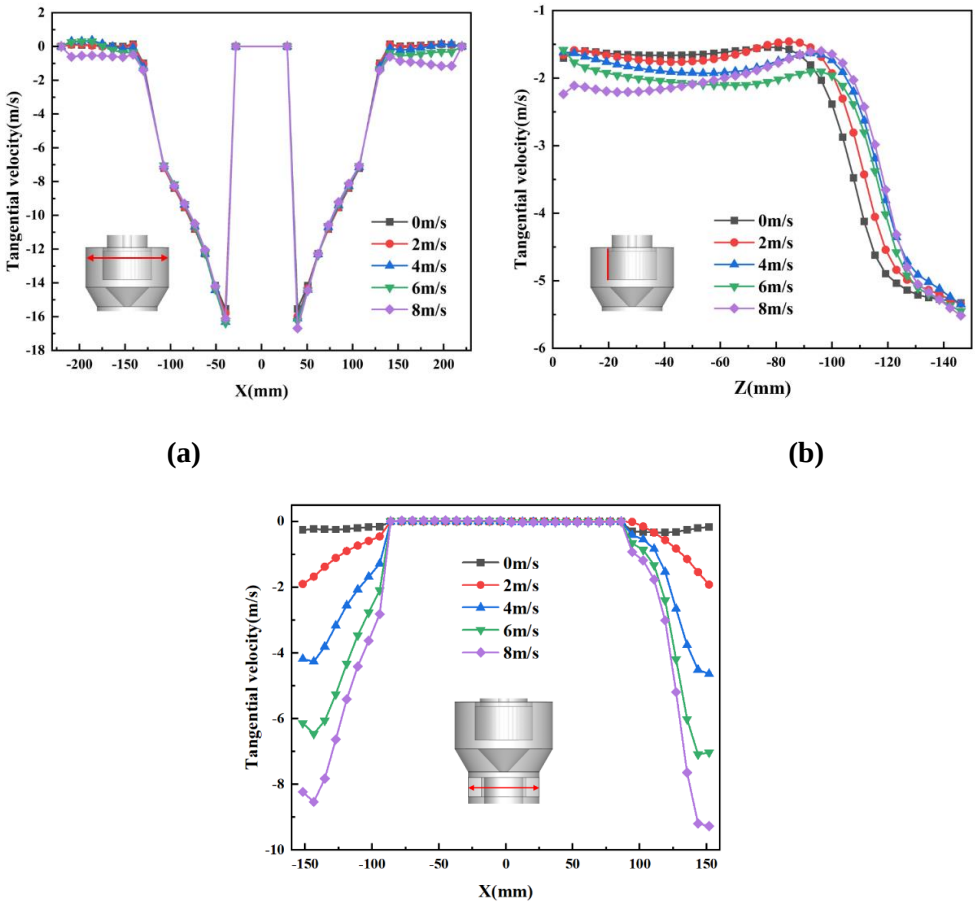

Fig. 6 Tangential velocity distribution.

3.2.2 Axial velocity distribution

Fig. 7 depicts the axial gas velocity cloud diagrams for different secondary gas velocity, and Fig. 7a to 7e correspond to the secondary gas velocities of 0, 2, 4, 6, and 8 m/s, respectively. As shown in Fig. 7a, in the area of the classification chamber, the downward axial gas velocity near the wall is responsible for transporting the coarse powder downward; the upward axial gas velocity near the rotor cage is responsible for bringing the fine powder upward and discharging it quickly inside the rotor cage, forming an obvious zero-velocity interface between the two. Note that Fig. 7b, c in the guide cone region and coarse powder recovery area also created the outer downward, and inner upward axial gas velocity. This establishes a conduit between the classification chamber, the guide cone zone, and the coarse powder recovery zone,

which assists in the descent of the coarse powder and the re-sorting of the entrained fines to increase classification accuracy. However, in Fig. 7d and Fig. 7e, the zero-velocity boundary is no longer evident, and the axial velocity is warped, which is produced by the high secondary gas velocity.

As can be seen from Fig. 8(a), with the change of the secondary gas velocity, the axial gas velocity near the wall of the classification chamber is between 1m/s and 2m/s. The maximum value increases and then decreases with the increase of the secondary air, which is favorable for coarse powder downward. In addition, the distance from the zero-velocity interface to the wall surface of the classification chamber also rises with the growth of the secondary gas velocity, and its variation spans from 17 mm to 40 mm. Fig. 8(b) depicts the axial velocity distribution at the edge of the rotor cage, and it can be observed that the axial gas velocity from the top to the bottom of the rotor cage tends to grow and then drop. The axial velocity achieves the highest value when the height of the rotor cage is 90mm-100mm, and this maximum value increases and subsequently declines with the growth of the secondary air, which allows the fine powder to be discharged swiftly.

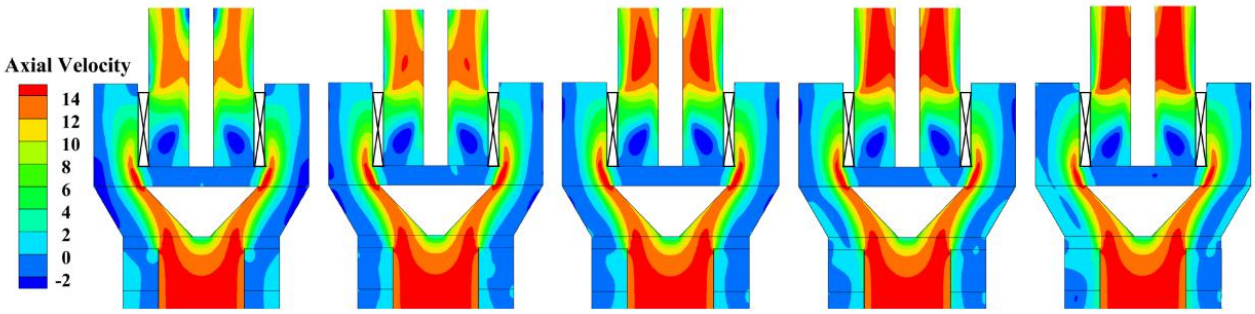

a b c d e

Fig. 7 The axial velocity cloud diagrams.

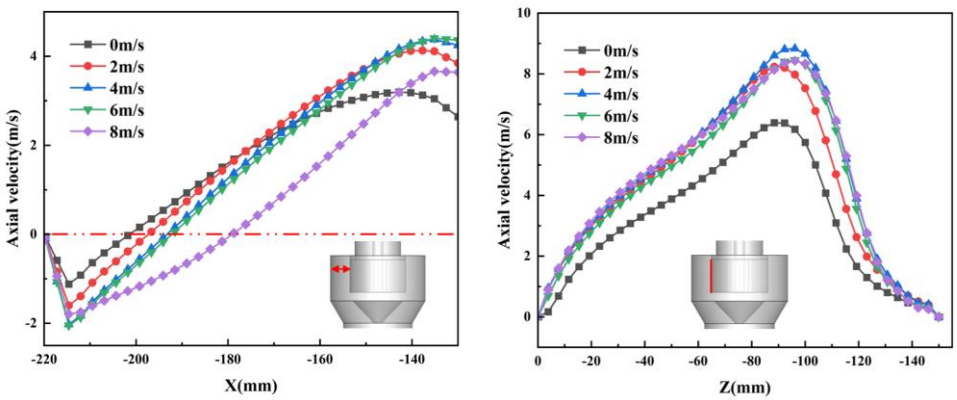

(a) **(b)**

Fig. 8 The axial velocity distribution.

3.2.3 Radial velocity distribution

Whether the radial gas velocity distribution is uniform or not is one of the elements impacting the classification accuracy, and Fig. 9 depicts the distribution of radial gas velocity. As shown in Fig. 9(a), the radial gas velocity is bigger in the middle and upper section of the rotor cage, suggesting that the airflow largely enters from the middle and top part of the rotor cage. Taking sites along the entry of the rotor cage, the radial gas velocity distribution is produced as illustrated in Fig. 9(b). When the radial gas velocity is negative, the airflow moves radially to the center of the rotor cage, which is the effective classification area, and it can be seen that the effective classification area increases with the increase of the secondary gas

velocity, but when the secondary gas velocity increases to a certain extent, the effective classification area no longer increases.

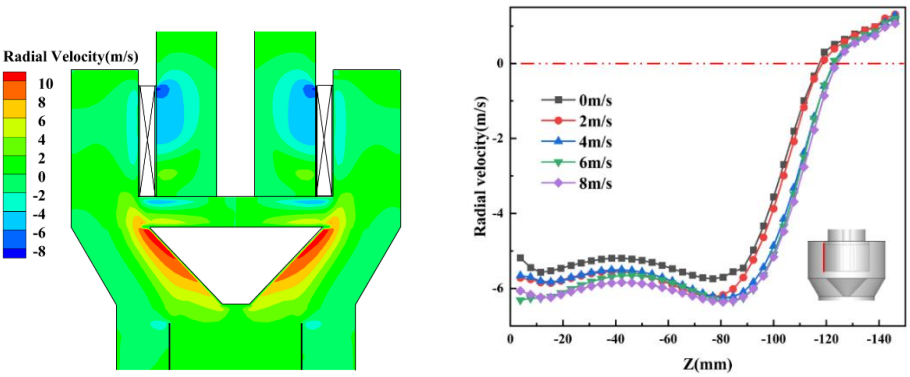

(a) (b)

Fig. 9 The radial velocity distribution.

3.3 Analysis of classification mechanism

To describe the classification mechanism of the NGZF classifier, the Discrete Phase Model (DPM) was built to simulate the particle trajectory, which can see the particle movement process more intuitively. In the NGZF classifier, the DPM model is employed to mimic the motion of the particle population. The particles of different sizes enter from the primary air inlet together with the primary air and arrive at the classification chamber to execute a rotating motion. The trajectories of the particles are illustrated in Fig. 10(a), and the motion trajectories of small and coarse particles are shown in Fig. 10(b) and Fig. 10(c), respectively. As can be observed by zooming in, the fine particles are flowing inward and obliquely upward, entering the rotor cage from the classification chamber and discharging swiftly. On the other hand, the coarse particles cannot enter the rotor cage, tend to flow diagonally downhill in the classification chamber, and fall fast to the coarse powder recovery region after approaching the wall.

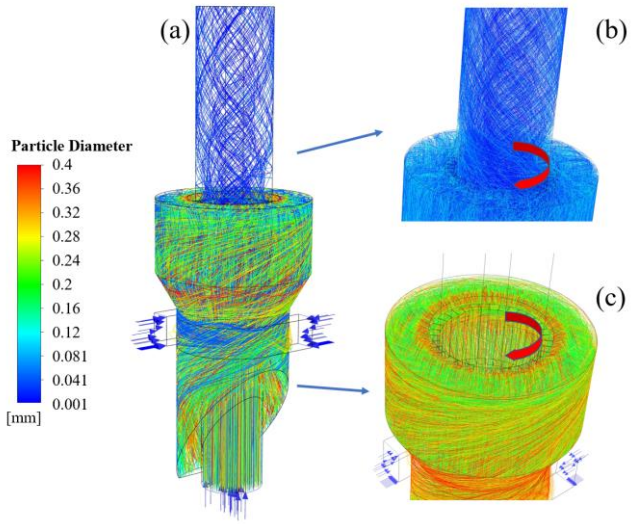

Fig. 10 Particle motion trajectory.

To further understand the impact of secondary air in the classifier, simulations were done for particles of three particle sizes. Fig. 11 depicts the trajectory of the particles on the X=0 surface, with the blue color representing the particles with a size of 5μm, the green color representing the particles with a size of 30μm, and the red color indicating the particles with a size of 70μm. It can be seen that 5μm particles deflected by the guide cone arrive at the powder selection region, owing to the tiny particle size, the centrifugal force is lower than the radial force, under the action of radial and axial forces straight into the rotor cage, and upward

collecting of fine powder. 70μm particles enter to the classification chamber, owing to the bigger particle size, the reverse radial force is larger, the combined effect of the force strikes the cylinder wall and flow downhill, and is collected as coarse powder. However, the 30μm particles first contact the cylinder wall and fall like the 70μm particles, but when they fall to the coarse powder recovery area, they will be re-screened under the action of the secondary air and come to the classification chamber for classification again.

Misclassification often exists in the actual classification process, and the secondary air can carry out reclassification of the particles that have been misclassified into the coarse powder collection area so that the misclassified particles can re-enter the classification chamber, to improve the classification accuracy.

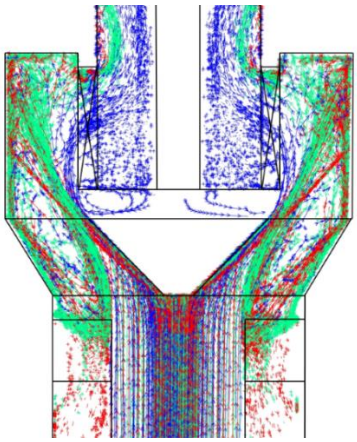

Fig. 11 Particle motion trajectory at X = 0 section.

4. EXPERIMENT PREPARATION

4.1 Experimental setup and material

As shown in Fig. 12a, the classification system of the experiment comprises an NGZF classifier, cyclone separator, baghouse dust collector, induced draft fan, and control system. In this experiment, the calcined petroleum coke was employed as the raw material, and the feed was roughly 1 kilogram for each experiment. The particle size of the powder sample was measured by utilizing a Bettersize2000 model laser particle size distribution meter, and the particle size distribution of raw material is displayed in Fig. 12b.

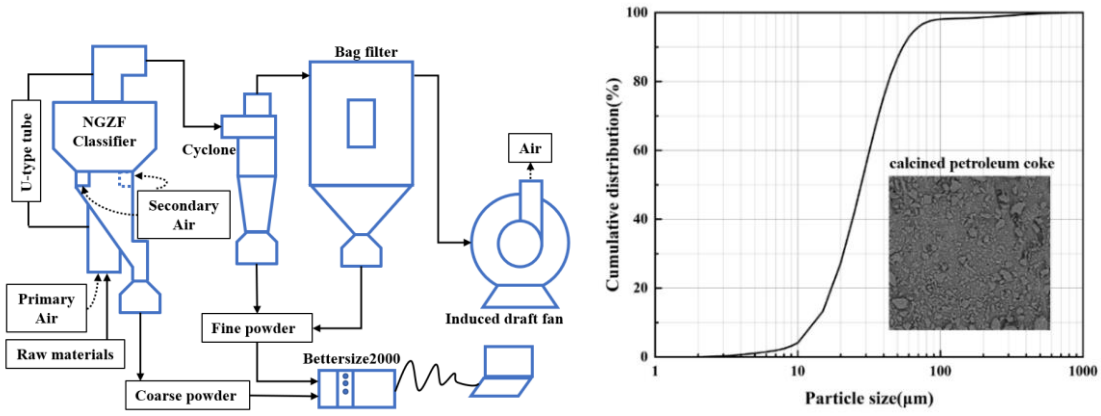

(a) (b)

Fig. 12 Schematic of the experimental setup(a) and particle size distribution of the raw material (b).

4.2 Classification performance indexes

The performance of the classifier is assessed using the cut size d_{50} and the classification accuracy *K*. The cut size d_{50} is the particle size at 50% partial classification efficiency, and the smaller the value, the

better the classification performance. Classification accuracy K is provided by the formula $K = \frac{d_{25}}{d_{75}}$, the bigger the value of K, the better the classification performance. The distinctive particle sizes of d_{25} and d_{75} are generated from the partial classification efficiency curves, which are numerically equivalent to the particle sizes corresponding to 25% and 75% of the curves, respectively.

5. EXPERIMENTAL RESULT AND ANALYSIS

5.1 Analysis of variance (ANOVA) and model fitting

Based on a one-factor experiment, the experimental data were analyzed using the response surface approach. According to the Box-Behnken experimental design concept, Design Expert software was applied to construct the tests for the rotor speed, primary air volume, and secondary air volume of the NGZF classifier. Using d_{50} and classification accuracy K as response values, 18 experiments were done, including 6 experiments at the center point. The intended three factors, three levels of response surface studies are illustrated in Table 1, with rotor speed (A), primary air volume (B), and secondary air volume (C) ranging from 800 to 1200 rpm, 400 to 600 $m^3 \cdot h^{-1}$, and 30 to 100 $m^3 \cdot h^{-1}$, respectively, to investigate the best operating conditions.

Table 1. Response surface experiment factors and levels.

Independent variables	ID	Levels		
		-1	0	1
Rotor speed(rpm)	A	800	1000	1200
Primary air volume($m^3 \cdot h^{-1}$)	B	400	500	600
Secondary air volume($m^3 \cdot h^{-1}$)	C	30	65	100

Table 2 provides the experimental d_{50} and K values. As can be observed from the table, d_{50} is inversely related to the rotor speed and directly proportional to the primary and secondary air, and the least d_{50} is just 28 μm. The classification accuracy K rises and then drops with the increase of each operating parameter. Therefore, to accomplish the requisite cut size and classification accuracy, the rotor speed and air volume must be matched.

The ANOVA findings for d_{50} and K are provided in Tables 3 and 4. The multivariate correlation coefficients, R2 of d_{50} and K are 99.48% and 99.41%, respectively, suggesting a high correlation. Their Adj R2 and Pred R2 values are high and both are extremely near to one other, indicating that the regression models fit d_{50} and K well and can effectively describe the sorting process. Adeq Precision is the ratio of effective signal to noise, and it is regarded as appropriate if it is more than 4. A CV of <10% for both implies that the accuracy and confidence of this experiment are excellent. The fitted regression equations for anticipated d_{50} and K are as follows:

d_{50}=72.50-18.00*A+18.75*B+8.00*C+5.00*AB+3.00*AC-1.50*BC-2.25*A^2-1.25*B^2-2.75*C^2

K=0.69-0.014*A-0.035*B-0.019*C-0.0075*AB+0.01*AC-0.0075*BC-0.072*A^2-0.050*B^2-0.038*C^2

Table 2. Design of experiments using BBD.

Runs	Independent variables			Responses	
	A	B	C	d_{50}	K
1	1000	500	65	95	0.54
2	1200	500	100	75	0.61
3	1000	400	100	61	0.56
4	1200	400	65	90	0.56

5	800	500	100	39	0.58
6	1000	500	65	39	0.65
7	1000	500	65	73	0.51
8	1000	500	65	75	0.69
9	1000	500	65	72	0.69
10	1000	400	30	28	0.59
11	800	500	30	74	0.69
12	1000	600	30	82	0.59
13	1000	600	100	73	0.7
14	800	400	65	70	0.69
15	800	600	65	80	0.62
16	1200	600	65	100	0.56
17	1200	500	30	58	0.63
18	1000	500	65	71	0.68

Table 3. ANOVA for the response surface regression of the d_{50}.

Source	Sum of Squares	Degree of freedom	Mean Square	F-Value	p-value
Model	6135.61	9	681.73	170.43	<0.0001
A	2592.00	1	2592.00	648.00	<0.0001
B	2812.50	1	2812.50	703.12	<0.0001
C	512.00	1	512.00	128.00	<0.0001
AB	100.00	1	100.00	25.00	0.0011
AC	36.00	1	36.00	9.00	0.0171
BC	9.00	1	9.00	2.25	0.1720
A2	22.09	1	22.09	5.52	0.0467
B2	6.82	1	6.82	1.70	0.2280
C2	33.00	1	33.00	8.25	0.0208

R^2=99.48%; Adj.R^2=98.90%; Pred.R^2=95.83%; Adeq Precision=49.31; CV=2.87%

Table 4. ANOVA for the response surface regression of the *K*.

Source	Sum of Squares	Degree of freedom	Mean Square	F-Value	p-value
Model	0.0630	9	0.0070	149.34	<0.0001
A	0.0015	1	0.0015	32.27	0.0005
B	0.0098	1	0.0098	209.07	<0.0001
C	0.0028	1	0.0028	60.00	<0.0001
AB	0.0002	1	0.0002	4.80	0.0598
AC	0.0004	1	0.0004	8.53	0.0193
BC	0.0002	1	0.0002	4.80	0.0598
A^2	0.0229	1	0.0229	489.31	<0.0001
B^2	0.0109	1	0.0109	232.73	<0.0001
C^2	0.0061	1	0.0061	130.91	<0.0001

R^2=99.41%; Adj.R^2=98.74%; Pred.R^2=95.13%; Adeq Precision=35.02; CV=1.11%

5.2 Effects of operational parameters

The three-dimensional response surface plots of d_{50} and K are presented in Fig. 12. which displays the influence of the interaction of two additional operational factors on d_{50} and K when one operating parameter is kept at a constant center value. From Fig. 12(a)~(c), it can be seen that when the primary and secondary air is constant, increasing the rotor speed increases the centrifugal force on the particles, which helps to reduce d_{50}, whereas when the rotor speed is constant and the primary and secondary air are increased, d_{50} increases, and the primary air has a greater effect on d_{50}. This is because the tangential gas velocity is mostly impacted by the rotor speed, whereas the axial and radial gas velocities are mainly affected by the air volume. From Fig. 12(d)~(f), it can be shown that under the condition of constant primary air volume and secondary air volume, the classification accuracy K displays a pattern of increasing and then dropping with the rise of rotor speed. Under the condition of maintaining the rotor speed fixed, the classification accuracy K also increases and then drops with the growth of primary air volume and secondary air volume. There is an essential interaction between the various operating parameters, thus it is required to optimize the operating parameters. In addition, it can be observed from the contours that d_{50} is substantially controlled by the rotor speed and the primary air, and the classification accuracy K is strongly influenced by each operational parameter.

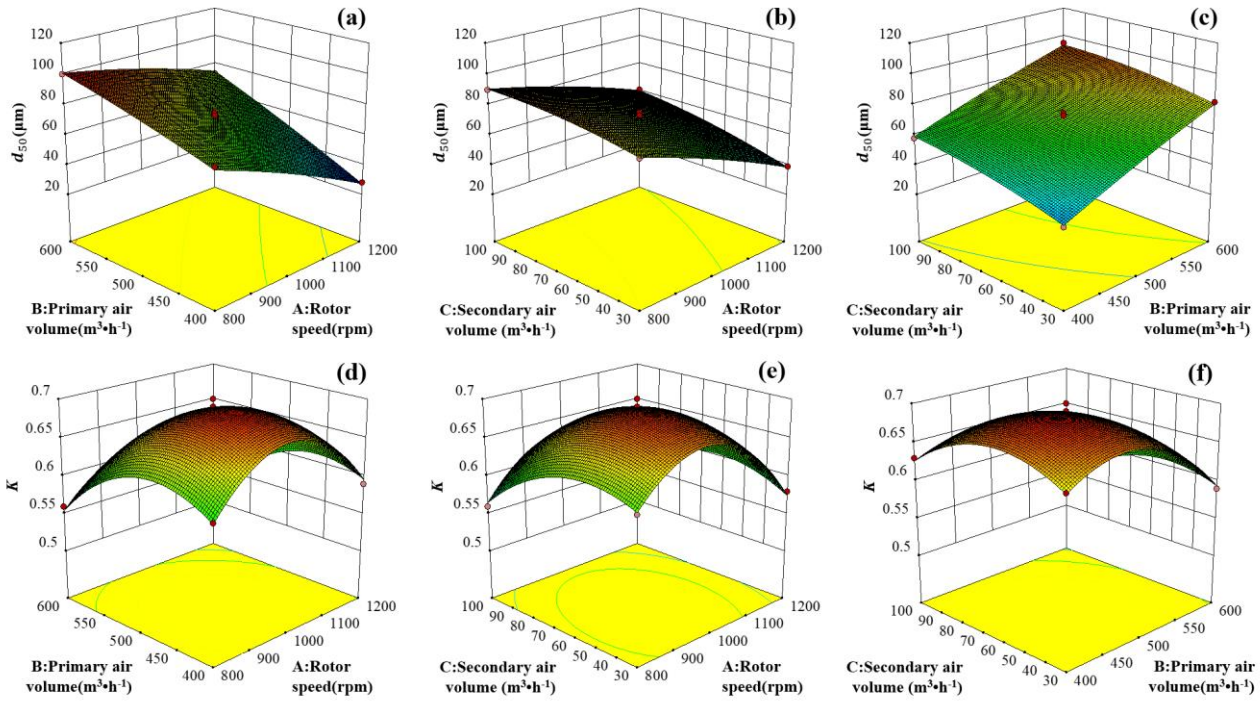

Fig. 13 2D and 3D response surface plots. (a)~(c): d_{50};(d)~(f): K

5.3 Optimization of operational parameters

The volume percentage of coarse particles (>50μm) in the final calcined petroleum coke was needed to be between 17% and 19%. The model was used to optimize for d_{50}=50μm and K maximum. The targeted objectives for each independent component and response are indicated in Table 5 and Fig. 14. The best working parameters of the classifier were rotor speed of 1037.4 rpm, primary air of 429.6 $m^3 \cdot h^{-1}$, and secondary air of 50.2 $m^3 \cdot h^{-1}$. The projected value of classification accuracy K for this operational parameter was 0.68 and the intended 0.957, which is close to the observed K value of 0.67. The d_{50} of the experiment is 50.41μm, which also validates the accuracy of the model.

Table 5. Operational parameters and responses used in the RSM.

Constraints	Goal	Lower limit	Upper limit
Rotor speed(rpm)	in range	800	1200
Primary air volume flow rate(m^3•h^{-1})	in range	400	600
Secondary air volume flow rate(m^3•h^{-1})	in range	30	100
d_{50}(μm)	target=20	28	100
K(-)	maximize	0.51	0.7

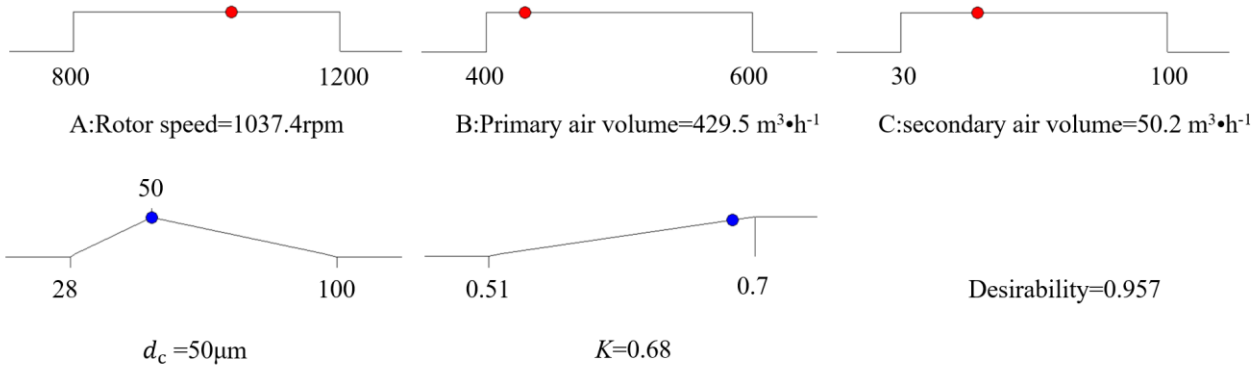

Fig. 14. Optimum operational condition for classifying calcined petroleum coke

6. CONCLUSIONS

In this research, ANSYS-Fluent 19.2 software was used to numerically model the NGZF classifier. The influence of secondary air on its internal flow field distribution and classification performance was explored and response surface tests using calcined petroleum coke were conducted and assessed. The following findings were drawn:

(1) After the secondary air reaches the NGZF classifier, it generates a phenomenon of spatial proximity control with the primary air and respective partition. The secondary air does not impact the tangential gas velocity in the classification chamber, and the washing flow field it generates does not interfere with the primary flow field generated by the primary air.

(2) The material initially enters the V-type classifier for pre-classified and pre-dispersion, and the primary classification location is in the NGZF classifier. When the air delivers the materials into the NGZF classifier for classification, the washing flow field generated by the secondary air can classify the misclassified particles again and enhance the classification accuracy.

(3) The classification chamber and guide cone region constitute the particle upward area and coarse particle descending area, and the contact between the two areas is clean. With the increase of the secondary air, the upward and downward velocities of the two regions increase, and the effective classification area in the classification chamber increases. However, when the secondary air is too large, it will produce turbulence to the axial velocity of the classification chamber and the guide cone zone, and the effective classification area is no longer improved.

(4) The results of the material experiment demonstrate that d_{50} is strongly impacted by the primary air volume and rotor speed, and the classification accuracy K is greatly influenced by each operational parameter. The proper combination of operating parameters may help the classifier achieve greater classification accuracy, and the operational parameters are rotor speed of 1037.4 rpm, primary air volume of 429.6 m^3•h^{-1}, and secondary air volume of 50.2 m^3•h^{-1}, and then classification accuracy K = 0.67.

References

[1] Karunakumari, L., *et al.*, Experimental and numerical study of a rotating wheel air classifier, *AIChE journal, 51*. (2005), 3, pp. 776-790, DOI No. 10.1002/aic.10349

[2] Shapiro, M.,V. Galperin, Air classification of solid particles: a review, *Chemical engineering and processing, 44*. (2005), 2, pp. 279-285, DOI No. 10.1016/j.cep.2004.02.022

[3] Guizani, R., *et al.*, Effects of the geometry of fine powder outlet on pressure drop and separation performances for dynamic separators, *Powder technology, 314*. (2017), pp. 599-607, DOI No. 10.1016/j.powtec.2016.10.025

[4] Yu, Y., *et al.*, Analysis of numerical simulation models for the turbo air classifier. , *Materialwissenschaft und Werkstoffechnik, 53*. (2022), 5, pp. 644-657, DOI No. 10.1002/mawe.202100130

[5] Sun, Z., *et al.*, CFD simulation and performance optimization of a new horizontal turbo air classifier, *Advanced powder technology : the international journal of the Society of Powder Technology, Japan, 32*. (2021), 4, pp. 977-986, DOI No. 10.1016/j.apt.2021.01.041

[6] Liu, R., *et al.*, Matching of air inlet velocity and rotor cage's rotating speed of turbo air classifier, *Hua xue gong cheng, 43*. (2015), 3, pp. 41-45, DOI No. 10.3969/j.issn.1005-9954.2015.03.011

[7] Zeng, Y., *et al.*, Numerical and Experiment Investigation on Novel Guide Vane Structures of Turbo Air Classifier, *Processes, 10*. (2022), 5, p. 844, DOI No. 10.3390/pr10050844

[8] Ren, W., *et al.*, Design of a rotor cage with non-radial arc blades for turbo air classifiers, *Powder Technology, 292*. (2016), 0, pp. 46-53, DOI No. 10.1016/j.powtec.2016.01.024

[9] Yu, Y., *et al.*, Effect of the rotor cage chassis on inner flow field of a turbo air classifier., *Materialwissenschaft und Werkstofftechnik, 52*. (2021), 7, pp. 772-780, DOI No. 10.1002/mawe.202000153

[10] Liu, R., *et al.*, Effects of axial inclined guide vanes on a turbo air classifier, *Powder technology, 280*. (2015), 0, pp. 1-9, DOI No. 10.1016/j.powtec.2015.04.034

[11] Zhao, H., *et al.*, Effects of the impeller blade geometry on the performance of a turbo pneumatic separator., *Chemical Engineering Communications, 205*. (2018), 12, pp. 1641-1652, DOI No. 10.1080/00986445.2018.1464918

[12] Yu, Y., *et al.*, A new volute design method for the turbo air classifier., *Powder Technology, 348*. (2019), 0, pp. 65-69, DOI No. 10.1016/j.powtec.2019.03.015

[13] Zhao, D.,S. Zhang, Effect of Volute Structure on Classification Performance of O-Sepa Classifiers, *China Powder Science And Technology, 21*. (2015), 6, pp. 20-24, DOI No. 10.13732/j.issn.1008-5548.2015.06.005

[14] Ren, C., *et al.*, Influence of air guide vanes on the flow field in a vortex air classifier, *Chemical Industry and Engineering Progress, 38*. (2019), 9, pp. 3988-3994, DOI No. 10.16085/j.issn.1000-6613.2018-2271

[15] Elsayed, K.,C. Lacor, The effect of cyclone inlet dimensions on the flow pattern and performance, *Applied mathematical modelling, 35*. (2011), 4, pp. 1952-1968, DOI No. 10.1016/j.apm.2010.11.007

[16] Yu, Y., *et al.*, Design of the new guide vane for the turbo air classifierDesign eines neuen Austrittsleitrads fur Turbo-Luftsichter, *Materialwissenschaft und Werkstofftechnik, 54*. (2023), 2, pp. 196-206, DOI No. 10.1002/mawe.202200108

[17] Yu, Y., *et al.*, The influence of air inlet layout on the inner flow field for a vertical turbo air classifier, *Physicochemical Problems of Mineral Processing*. (2023), pp. 175859-175873, DOI No. 10.37190/ppmp/175859
[18] Yu, Y., *et al.*, Influence of guide vane on dispersion of aggregates near the guide vane in a turbo air classifier, *Powder technology*, *434*. (2024), p. 119344, DOI No. 10.1016/j.powtec.2023.119344
[19] Lin, T., *et al.*, Exploring the factors affecting the efficiency of the O-Sepa separator, *China Cement*. (2020), 7, pp. 95-97
[20] Li, B., *et al.*, Development and application of DS-M type ultra-subdivisional sorting machine, *Cement engineering*. (2020), 3, pp. 33-35, DOI No. 10.13697/j.cnki.32-1449/tu.2020.03.011
[21] Sun, J., *et al.*, Structural analysis and improvement of the O-Sepa powder separator, *Cement*. (2013), 2, pp. 35-37, DOI No. 10.13739/j.cnki.cn11-1899/tq.2013.02.026
[22] Ren, C., *et al.*, Effect of air guide vanes on the flow field in a vortex air classifier, *Chemical progress*, *38*. (2019), 9, pp. 3988-3994, DOI No. 10.16085/j.issn.1000-6613.2018-2271
[23] Xu, H., Improvement of unreasonable air inlet duct arrangement of O-Sepa separator, *Cement*. (2012), 10, pp. 61-62, DOI No. 10.13739/j.cnki.cn11-1899/tq.2012.10.034
[24] Li, Q., *et al.*, Effects of a Guide Cone on the Flow Field and Performance of a New Dynamic Air Classifier, *Processes*, *10*. (2022), 5, p. 874, DOI No. 10.3390/pr10050874
[25] Mou, X., *et al.*, CFD-Based Structural Optimization of Rotor Cage for High-Efficiency Rotor Classifier, *Processes*, *9*. (2021), 7, p. 1148, DOI No. 10.3390/pr9071148
[26] Jia, F., *et al.*, A new rotor-type dynamic classifier: Structural optimization and industrial applications, *Processes*, *9*. (2021), 6, p. 1033, DOI No. 10.3390/pr9061033
[27] Braun, R.M., *et al.*, Fine dry comminution of calcium carbonate in a Hicom mill with an Inprosys air classifier, *Minerals engineering*, *15*. (2002), 3, pp. 123-129, DOI No. 10.1016/S0892-6875(01)00217-5
[28] Zeng, C., *et al.*, Effects of secondary air on the classification performances of LNJ-36A air classifier, *Chemical Industry and Engineering Progress*, *34*. (2015), 11, pp. 3859-3863, DOI No. 10.16085/j.issn.1000-6613.2015.11.006
[29] Wei, L.,M. Sun, Numerical studies of the influence of particles' size distribution characteristics on the gravity separation performance of Liquid-solid Fluidized Bed Separator, *International journal of mineral processing*, *157*. (2016), pp. 111-119, DOI No. 10.1016/j.minpro.2016.10.004
[30] Sun, Z., *et al.*, Experimental and CFD study on a cyclonic classifier with new flow pattern, *Advanced powder technology : the international journal of the Society of Powder Technology, Japan*, *30*. (2019), 10, pp. 2276-2284, DOI No. 10.1016/j.apt.2019.07.007
[31] Petit, H.A., *et al.*, Evaluation of the performance of the cross-flow air classifier in manufactured sand processing via CFD–DEM simulations, *Computational particle mechanics*, *5*. (2018), 1, pp. 87-102, DOI No. 10.1007/s40571-017-0155-6
[32] Sun, Z., *et al.*, CFD simulation and optimization of the flow field in horizontal turbo air classifiers, *Advanced Powder Technology*, *28*. (2017), 6, pp. 1474-1485, DOI No. 10.1016/j.apt.2017.03.016
[33] Hui, C., *et al.*, CFD simulation and performance study of a three-separation combined air classifier, *Thermal science*. (2023), pp. 183-183, DOI No. 10.2298/TSCI230513183H

Submitted: 24.3.2024.
Revised: 12.5.2024
Accepted: 23.5.2024.